Research Square

Preprints are preliminary reports that have not undergone peer review.
They should not be considered conclusive, used to inform clinical practice,
or referenced by the media as validated information.

Flood-related surface collapse at Osuga Valles: Subsurface salt dissolution on Mars?

Itay Halevy

itay.halevy@weizmann.ac.il

Weizmann Institute of Science https://orcid.org/0000-0002-7325-8139

Roy Naor

Weizmann Institute of Science

Virginia Gulick

University of Arizona, Tucson

Amit Mushkin

Geological Survey of Israel

Article

Keywords:

Posted Date: July 15th, 2025

DOI: https://doi.org/10.21203/rs.3.rs-6992765/v1

License: This work is licensed under a Creative Commons Attribution 4.0 International License. Read Full License

Additional Declarations: There is **NO** Competing Interest.

Version of Record: A version of this preprint was published at Communications Earth & Environment on June 20th, 2026. See the published version at https://doi.org/10.1038/s43247-026-03683-w.

Abstract

Constraining the formation mechanism of geologic depressions on the surface of Mars can shed light on the planet's climatic, hydrological, and geochemical evolution. At Osuga Valles, surface morphologies indicative of catastrophic flood events can be tracked from their chaotic origins down to their sink at terminal depressions, or cavi. The channel-cavi morphological association suggests a genetic link between inflowing floodwater and cavi formation and evolution. The geologic settings are consistent with a pre-flood, evaporite-containing sedimentary basin. Estimates of the water volumes associated with the Osuga Valles floods suggest cavi formation within this sediment-filled basin by surface collapse into voids generated by dissolution of subsurface magnesium sulfate minerals, which are commonly detected in the region. Geologic mapping reveals that initial cavi collapse was associated with floodwaters from relatively low-discharge floods, which likely infiltrated the subsurface through fractures. Subsequent higher-discharge floods drained directly into the evolving cavi, causing further dissolution and collapse.

Introduction

Key constraints on the climatic history and habitability of Mars hinge on studies of the planet's surface and inferred understanding of its subsurface environment[1–3]. The paucity of direct subsurface observations on Mars can be partially addressed by interpreting the surface expression of subsurface processes, as is often done in the case of geologic depressions on Earth[4–6]. Geologic depressions that are not impact-related are common on Mars and are broadly defined as topographic lows formed by either explosion or collapse due to substrate volume loss[7–12]. Martian depressions of various shapes, sizes, and morphologies have been linked to numerous formation mechanisms including magmatism, tectonic processes, cryosphere withdrawal and aquifer breach, dehydration of clays and dissolution of sedimentary salts[12–15].

The occurrence of salts in the sedimentary record of Mars provides one of the central lines of evidence for an early warm and wet climate[1, 2, 16, 17]. The salts most commonly detected on the surface of Mars are sulfate minerals[18–20], but the surface exposure of such salts may provide only glimpses into a wider distribution in the subsurface. A better understanding of the type, volume, and spatial distribution of ancient salts on Mars may help constrain the history of the planet's coupled climate, geochemistry, and potential habitability.

Multiple independent observations suggest the existence of an ancient sedimentary basin buried under kilometers of mostly volcanic units of the Tharsis bulge and adjacent terrains. For example, thick sulfate-rich sedimentary units exist within Valles Marineris and within adjacent chasmata, such as Juventae Chasma and Hebes Chasma[20–22]. The existence of the chasmata themselves requires mobilization of large volumes of material and the dissolution of subsurface salts (and subsequent collapse of overlying rocks) is one of the proposed mechanisms[23]. In addition, dewatering of subsurface hydrated evaporites was proposed as the source of mega outflow channel systems[21]. While the spatial extent of such buried salts is unclear, the boundaries of a primordial ocean or sea proposed to have occupied the northern lowlands[24–28] may provide a rough estimate for their distribution.

Under certain conditions, salts can dissolve in the Martian subsurface to form voids[29]. The existence of depressions with indications of collapse into such voids may thus help constrain the subsurface distribution and characteristics of purported buried salt units susceptible to dissolution. Since both the formation and dissolution of such deposits requires liquid water, knowledge of their distribution and properties informs the planet's climatic and hydrological past. Occurrences of Martian depressions far from volcanic vents and in association with buried salt deposits overlain by volcanic rocks have indeed been reported[9, 27, 30] and in some cases, suggestions for their formation involve collapse into subsurface salt dissolution voids[9, 13, 14, 31]. Furthermore, depressions ranging from a few meters to a few hundred

meters in scale have been detected within sulfate outcrops on low-latitude Martian surfaces and were suggested to have formed by dissolution of the sulfate salts[32–36]. The potential ubiquity of such geologic settings motivates further investigation of a depression formation mechanism by surface collapse into subsurface salt dissolution voids.

Here, we focus on the Osuga Valles system near the eastern edge of Valles Mariners (Fig. 1), which provides an opportunity to study multi-kilometer-scale depressions with an origin that appears related to aqueous processes, rather than volcanic or structural origins. The distinctive catastrophic outflow system of Osuga Valles can be tracked from its chaotic origins, through flood channels, down to its sink at terminal, closed-basin depressions[15, 37], which we hereafter term Osuga Cavi (name request was submitted to the IAU WGPSN). The morphological association between the cavi and the channels that drain into them suggests a genetic link between the inflowing flood water and cavi formation. Specifically, this genetic association indicates a possibility of cavi formation by surface collapse in response to subsurface dissolution processes. In work on flood-related subsidence of sinkholes along the Dead Sea shores, it has been speculated that such an association may be found on Mars[4], where evaporite sequences and mega-floods are observed in the geologic record[1,38]. Thus, the study of Osuga Valles may contribute to our understanding of possible salt dissolution mechanisms in the formation of depressions on Mars and help to constrain subsurface stratigraphy. Furthermore, the understanding that surface data can shed light on subsurface properties and processes is highly relevant for planetary research in general, where most of the information available comes from remote sensing of the surface.

Results and Discussion

Two major regional structures govern the pre-outflow topography and the distribution of subsurface planes that may have served as hydraulic conduits (Fig. 2). First, two of the outer ringed ridges of the multi-ring impact structure of the Ladon Basin (Fig. 2A)[39–42] broadly divide the study area into three topographic stairs of eastwards decreasing elevation into the basin (Fig. 2B-C). Second, the stairs are dissected by a set of generally E-W trending fractures associated with Valles Marineris and its stress field[40, 43]. One of these fractures appears to divide the lowermost stair into a northern subsided block and a southern raised block (Fig. 2B and D). Superposing this large-scale landscape are multi-terraced valley networks that occur on the steeper slopes of the middle topographic stair and the raised block of the lowermost stair. The valley networks dissipate at the transition to the subsided block of the lower topographic stair (Fig. 2B, D and E; see Ref. 40 and references therein for general review on valley network behavior in this region of Mars). The dissipation of the valley networks at the subsided block, as well as the more moderate slopes and lower relief on this block (Fig. 2B and D), suggest that this topographic low may have been the locus of a sedimentary basin that predated the Osuga Valles flood events (Fig. 3), consistent with previous work[37]. The possible existence of a sedimentary basin in association with the lower stair is supported by additional observations along the ringed ridge that separates the middle from the lower stairs. These observations suggest that the subsurface of the lower stair is mechanically different from that of the middle stair, as would be the case if the lower stair were sediment filled. For example, in the Tigre Valles (TV) system, ~ 120 km to the north of the Osuga system, outflow channels in the middle stair terminate at the transition to the lower stair where they are cut by what appears to be a collapse morphology (Fig. 2B). Further north and east along the transition between the middle and lower stair, the boundary of Aurora Chaos (AC) forms an embayment into the lower stair, again suggesting that the subsurface of the lower stair was less resistant than the middle stair against the processes that formed the chaos (Fig. 2B).

The valley networks and the proposed sedimentary basin are crosscut by the Osuga Valles system (Figs. 2E and 3). From a regional perspective, three morphologically distinct segments in the Osuga Valles system correspond to the three regional topographic stairs. On the upper of these stairs, two distinct zones of chaotic terrain appear to be the origin of convoluted flood channels that cut through the middle stair (Figs. 2B, 2D, 3, and 4). Crosscutting relations imply

that the later outflow event originated from the southern zone of the chaotic terrain, postdating outflows from the northern zone of the chaotic terrain (Fig. 4B). In the convoluted channel segment on the middle stair, shallower channels are crosscut by deeper and wider channels (Fig. 4C), suggesting that the later outflow events produced higher discharges (Fig. 4B). Before the channel system terminates at Osuga Cavi, the deeper and wider channels merge to flow through preexisting E-W fractures that breach the ringed ridge down to the sedimentary basin on the lower stair and possibly into its subsurface, where the cavi presently occur (Fig. 4). The merging of the channels occurs at a ~ 500 m cataract-like elevation step (Fig. 4D), from where the merged channel descends gradually (i.e., without clear topographic steps) into the westernmost cavus. Formation of this cavus postdates the earliest flows, which are marked by lower-discharge channels on the surface above the main merged channel (Fig. 4D). These channels record an earlier higher-elevation base-level, the existence of which is supported by observations of remnant fluvial morphology on some of the slumped blocks in the cavi (Fig. 4E). Irrespective of the existence of a higher-elevation basin, the location of the cataract suggests a drop in base level followed by cataract retreat likely associated with subsequent flood events.

The Osuga Cavi complex is composed of a set of individual depressions (Figs. 2D, 3, 4A and 5A). A major cavus ("primary" cavus), with irregular outline in map view, comprises about half of the cavi area (the western half). Remnants of the primary cavus' original floor are cut by a deeper "nested" cavus (Figs. 4D and 5A). The total relief from the plain of the lower topographic stair (i.e., outside the cavi) to the lowermost point in the cavi is ~ 2,800 m, about half of which is attributed to the primary cavus and half to the nested cavus. The merged outflow channel gradually descends eastwards onto the primary cavus floor, which presents fluvial morphologies that are related to the latest flood events (Fig. 4D). These morphological observations suggest direct flow of water into the primary cavus. Moreover, a diversity of sedimentary morphologies in the primary cavus (Figs. 5, 6 and S1) may postdate this cavus formation and be remnants of deposition by the flood waters. The absence of flow features exiting the primary cavus suggests that the flood waters that entered the cavus either evaporated, froze and then sublimated, or drained into the subsurface. The rest of the Osuga Cavi complex, comprises shallower (≤ 2,200 m deep), overlapping individual depressions ("peripheral" cavi), which mostly display concentric patterns of collapse (Fig. 5A). These patterns, together with the absence of surface flow features that exit these peripheral cavi, suggest that they formed by collapse into missing subsurface volume.

The mapped morphologic relations between the channels and cavi suggests that multiple phases of surface water flows in the channel segment drained into the subsurface at or near the terminal cavi current location and resulted in surface collapse within the cavi complex. Time-progressive base-level drop for the channel segment is supported by the existence of an early higher-elevation basin and the cataract at which the channels merge (Fig. 4A and D). Evidence for the higher-elevation basin includes the shallow, low-discharge channels near the primary cavus' western rim that are cut by the deeper merged channel (Fig. 4D), and the remnant fluvial morphology on some of the slumped blocks within the cavi (Fig. 4E). No shallow, low-discharge channels are observed immediately east of the cavi. This suggests that the water that flowed in the western channels, prior to the cavi's formation, did not continue to flow on the surface and possibly drained into the subsurface of the early higher-elevation basin. This sequence of events appears to have predated the collapse of the primary cavus, and we suggest that flow events postdating the primary cavus formation also resulted in drainage of water into the subsurface and subsequent collapse. In support of this hypothesis, the nested cavus cuts both the primary cavus bottom and the fluvial features on its floor associated with the last flood events (Figs. 4 and 5), suggesting that the collapse of the nested cavus postdated these floods. The flood waters entered the primary cavus but did not exit by overland flow. We suggest that their drainage into the subsurface may be related to formation of the nested cavus'. Blocks within the nested cavus, which display sedimentary layering (Fig. 6), appear to be collapsed remnants of the primary cavus floor, suggesting (*i*) the existence of a sedimentary basin within the primary cavus, and (*ii*) possible drying and induration of the sediments within this basin prior to the collapse of the nested cavus. As in the case of the nested cavus, we further suggest that the missing subsurface volume into which the peripheral cavi apparently collapsed is related to drainage of water from the primary cavus into the subsurface.

Support for cavi collapse at Osuga in response to surface flows that terminated within the cavi and drained into their subsurface can be found in a terrestrial analog site located near the Dead Sea in southeastern Israel where sinkhole clusters morphologically resemble the Osuga Cavi complex[44]. In general, sinkhole formation along the Dead Sea shores is associated with subsurface dissolution of a meters-thick late Pleistocene salt layer that is buried under a few tens of meters of relatively insoluble mud or alluvial sediments[45]. Dissolution and loss of this subsurface salt volume ultimately results in collapse of the overlying sediments to form sinkholes that are meters to tens of meters in diameter and several meters to a few tens of meters deep[45–47]. Most of the subsurface salt dissolution along the Dead Sea shores is driven by intrusion of fresh groundwater into local salty aquifers in response to lake level drop of ~ 1 m/year during the past ~ 30 years. However, the evolution and post-collapse growth of a subset of Dead Sea sinkhole clusters that occur within the Ze'elim alluvial fan appears to be dominated by drainage of overland flash-flood waters directly into the sinkholes (Figs. 7 and S2)[44]. There, flood waters captured into initial sinkholes are directly routed into the subsurface to become the locally dominant dissolution agent of the buried salt unit. This process greatly enlarges existing sinkholes over time with multiple flood events progressively promoting new sinkhole formation in adjacent areas (Figs. 7 and S2)[4, 44, 48, 49]. More generally, it has been shown that the growth rate of Dead Sea sinkholes is highest in the vicinity of surface water flows[4, 48]. The size of the Ze'elim sinkholes, which is controlled by the thicknesses of salt layer being dissolved and the overlying sediments, is approximately three orders of magnitude smaller than that of the Osuga Cavi. However, it appears conceivable that dissolution of salt layers that are hundreds to thousands of meters thick on Mars[21, 22, 50, 51] by the large volumes of water associated with Martian mega-floods[52], could result in collapse pits that are hundreds to thousands of meters in diameter and depth[9].

The location of flow and collapse features in the Osuga system appears to follow preexisting structures, namely the topographic stairs defined by the ringed ridges of the Ladon Basin and the superposed E-W trending fractures that dissect the stairs. The collapse features are restricted to part of the lower (eastern) topographic stair. They are bounded to the west by the ringed ridge, and to the south by the E-W scarp that separates the subsided (north) and raised (south) blocks of the lower stair (Figs. 2 and 3). Demonstrating further structural control on the Osuga system, the convoluted channels merge and breach the ringed ridge in association with the E-W fractures (Figs. 2 and 3). The crossing of two major planes of weakness—the fault between the ringed ridge and the lower stair (which is also a contact between bedrock and sediments), and the E-W fractures—may have facilitated the flow of water into the subsurface. If the evaporites were deposited after the formation of the multi-ring Ladon Basin, then the impact-induced tilted block structure of the basin suggests that water likely infiltrated the subsurface at the approximate location of maximal evaporite thickness (i.e., closest to the fault). Formation of a subsurface void at this location and the upward propagation of subsurface deformation may explain the location of the cavi and the absence of similar features upstream (on the middle stair). That is, in other locations, surface collapse did not occur because of the absence of thick, soluble sediments in the subsurface and/or the absence of suitable conduits for water flow into the subsurface.

Based on the above observations and analogy with the Ze'elim alluvial fan sinkholes, we suggest the following chain of events for the formation of the Osuga system (Fig. 8). An evaporite sequence several kilometers thick was deposited within a regional-scale basin. The evaporite units either (*i*) predate the pre-Noachian formation of the Ladon Basin[53] and were deformed by the impact that formed the basin, or (*ii*) postdate Ladon Basin formation and deposited in the topographic lows related to the multi-ring basin (e.g., the troughs between the ringed ridges). These two formation scenarios also bear on the spatial extent of the evaporites, which is at present unclear. If the evaporites formed in association with a proposed northern ocean, they may be related to other evaporite sequences documented to underlie the Tharsis bulge and other volcano-regolith sequences[21]. In this case, existence of evaporites in the subsurface of the lower stair may constrain the spatial extent of the northern ocean, the southern shorelines of which have been buried or destroyed in the study region[27, 28].

Irrespective of their spatial extent and depositional environment, the evaporite units were subsequently covered by an unknown thickness of insoluble units (e.g., volcanic or siliciclastic rocks; Fig. 8A). Catastrophic outflows then originated at the higher elevations of the upper (western) stair occupying the outer of the two ringed ridges of the Ladon Basin in the Osuga study region. The outflows carved convoluted channels on the surface of the middle stair and breached the inner of the two ringed ridges at the study site to flow down to the lower stair by utilizing a set of preexisting E-W fractures (Fig. 8B1). The intersection of the E-W fractures and the fault associated with the ringed ridge resulted in locally optimized surface-subsurface connectivity and a weakening of the insoluble roof. The unique occurrence of surface flow at this intersection, which was located at the margin of the buried evaporite sequence, triggered volume loss by salt dissolution (Fig. 8B2), which led to initial surface collapse and formation of the primary cavus (Fig. 8C). We cannot rule out some subsurface dissolution by groundwater prior to the catastrophic outflow events, though we find no morphological evidence for such pre-outflow dissolution. Subsequent outflow events, higher in discharge, drained directly into the depressions forming at the lower stair (Fig. 8D). These flood events caused cataract retreat into the middle stair, enlargement of the existing depressions, temporary pooling in the primary cavus, and deposition of sediments. Infiltration of flood waters into the subsurface caused additional salt dissolution, growth of the existing cavi, and formation of new cavi (the peripheral cavi). Following the desiccation of the sediments in the primary cavus, the last flows probably entered a dry cavus and extended the dissolution downward, ultimately causing the collapse of the nested cavus after the flood terminated (Fig. 8E).

Additional support for the hypothesis of Osuga Cavi formation by dissolution of subsurface salts was obtained from order-of-magnitude agreement between estimates of (*i*) the volume of salt proposed to have dissolved and (*ii*) the volume of water available for such dissolution. Both volumes were constrained by the volume of missing substrate in the channel segment and the cavi complex segment of Osuga. The volumes of substrate removed were estimated as the elevation difference between the MOLA DTM and an interpolated pre-outflow capping surface (Methods; Fig. S3), integrated over the area within the segment boundaries (Fig. 9). Estimates of the uncertainty in the volumes of all system segments are associated with the manual choice of segment boundaries. The measured cavi volume (best estimate 1417 km^3, range 1257–1539 km^3) provides an estimate of the volume of salt proposed to have dissolved in the subsurface. This estimate is approximate, because the surface expression of the subsurface volume loss is affected by additional and poorly constrained factors, such as (*i*) the fraction of soluble and insoluble materials in the evaporite-bearing units, (*ii*) dilation of the collapsed material, (*iii*) post-collapse aeolian or glacial deposition in the cavi, (*vi*) alluvial transport within and beyond the system, and (*v*) loss of subsurface volatiles. As described in the Methods, a conservatively low estimate of the volume of water available for dissolution comes from the channel segment of the Osuga system (best estimate 931 km^3, range 926–959 km^3) and a conservative assumption of 5–20% sediment load. The resulting volume of water is ~ 3700–18200 km^3. The lower end of this range is comparable to the volume of the chaotic regions (best estimate 3122 km^3, range 2919–3365 km^3). We note that the water can originate from a region larger than the areal extent of the chaotic regions.

Using the reported solubility of a variety of salts observed on Mars or proposed to have formed on the planet's surface (Table S1), we calculated the volume of salt that would be dissolved by the above estimate of the volume of water (Methods). Under an assumption of sufficient residence time of the water in contact with the subsurface salt to reach saturation with respect to the salt, the volume of a specific salt that can be dissolved by the volume of water depends on that salt's solubility and density. Implicit in the assumption of saturation is that this is an upper limit on the salt volume but recalling that the water volume estimate is conservatively low, we consider the uncertainty on the resulting salt volume estimate to be acceptable. We find that only dissolution of magnesium sulfate minerals consistently yields subsurface volume loss nearly sufficient to account for the observed volume of the cavi (Fig. 10). If the water volume were higher than our conservative lower estimate by a factor of only ~ 1.5–1.8, then dissolution of magnesium sulfates can explain the entire observed volume of the cavi. Alternatively, the difference can be explained by fluidization of an

insoluble fraction by the subsurface flow or sublimation of subsurface ice exposed by the collapse. Calcium carbonate minerals yield sufficient volume, but only if the pH of the infiltrating solution was ~ 2. Such low pH could occur, for example, if the solutions emanating from the chaotic origin terrains contained ~ 5 mM unneutralized sulfuric acid, which is unlikely in solutions with a subsurface origin. Alternatively, a pH of ~ 2 would be achieved by oxidation and hydrolysis of ~ 10 mM ferrous iron upon exposure to Mars' atmosphere, but the solubility of most ferrous iron minerals would preclude such high dissolved iron concentrations. These considerations, together with the scarcity of carbonate minerals on the surface of Mars[17, 54], suggest magnesium sulfate minerals as the most likely candidates to explain the subsurface volume loss that led to formation of Osuga Cavi. Indeed, sulfate minerals observed in outcrops in the relative vicinity of the Osuga system (e.g., Capri Chasma ~ 500 km away, Arisinoes Chaos ~ 650 km away, Aureum Chaos ~ 850 km away, Juventae Chasma ~ 1500 km away, Coprates Chasma ~ 1800 km away, Meridiani Planum ~ 2,000 km away) are consistent with magnesium sulfates[20, 22, 50, 51, 55, 56]. These outcrops are additionally equivalent in thickness and in absolute elevation (of the exposures) to Osuga Cavi's elevation and total depth[57].

Our mapping and crater counting model surface ages reported in another study[58] agree with the sequence of events proposed above (i.e., repeated episodes of flow and subsequent collapse, separated by long dry intervals). Although such model surface ages typically have large non-modeled uncertainties, especially when calculated for relatively small surface areas like those in the channels and cavi, consistency with other geologic observations in this study supports the crater ages. The crater counting statistics yield an Early Hesperian age (~ 3.6 Ga)[58] for the basin on the lower stair's subsided northern block, which is cut by Osuga Cavi (Terra Depositional; Fig. 3). A similar age (~ 3.5 Ga)[58] was determined for the higher-elevation terrains surrounding this basin (i.e., the upper and middle stair and the elevated southern block of the lower stair; Terra Erosional; Fig. 3). Further confidence in the crater counting ages is provided by this similarity in the ages of pre-outflow surfaces, which is expected because the higher and lower terrains are genetically linked as an erosional watershed and its associated depositional basin, respectively. The crater counting model ages are also consistent with the mapped continuation of these units in adjacent quadrangles[59, 60]. Since Ladon Basin has been dated to ~ 4.2 Ga[61], the crater counting model ages[58] determined for the pre-outflow surfaces imply that the (putatively sulfate) sediments in the subsurface of the lower stair are older than ~ 4.2 Ga if they predated Ladon Basin, or that they are aged ~ 4.2 to ~ 3.6 Ga if they postdate Ladon Basin and were deposited within topographic lows associated with the basin's ringed ridge structure. The latter of these age ranges is consistent with proposed ages of sulfate mineral deposition on Mars[1], though it is not possible to rule out deposition of sulfates earlier in Mars history and their repeated remobilization until the planet's surface froze and became desiccated[62, 63].

The model ages for the channels in the middle stair vary widely but are consistently younger than ~ 1.9 Ga (ref. 58), suggesting that outflow events in Osuga Valles initiated in the Middle Amazonian. The geomorphologically latest channels are as young as ~ 100 Ma (ref. 58), and even considering non-modeled uncertainties in these ages, they strongly suggest that the latest outflow events occurred in the Late Amazonian. These findings are consistent with the crater age studies of some of the largest outflow channels in southern circum-Chryse, whose activity peaked during the Middle Amazonian[64]. The Osuga channel ages[58] are also consistent with a previous study in which it was suggested that the adjacent Tigre Valles, just ~ 120 km to the north of Osuga Valles, is aged ~ 1 Ga (ref. 15). The cavi's model ages suggest that they are as young as, and possibly younger than the channels associated with the specific flows that induced specific collapse events of the terminal cavi.

If, as we suggest, Osuga Cavi formed as a result of subsurface salt dissolution, our mapping and the crater counting model ages[58] indirectly constrain the spatial distribution of Hesperian or earlier salt deposits and directly support suggestions of large-scale drainage of the Martian hydrosphere during the Amazonian[64]. While Osuga Cavi may be special in their clearly observed flood-collapse association, their pre-collapse stratigraphy and/or formation mechanism may be more common. Other large depressions on Mars may have formed by salt dissolution and may thus imply a vast

evaporitic record that could account for the missing salts expected to have formed on a warm, wet, clay-producing early Mars[62].

Conclusions

We explored a possible subsurface salt-dissolution formation mechanism for Osuga Cavi, a tightly clustered and nested set of depressions on Mars (centered around 14°50'S and 37°25'W), which occurs at the outlet of catastrophic outflow channels (Osuga Valles). A hypothesized link between cavi formation and the inflowing flood water was confirmed by mapping, photogeology, and crater-counting model ages, all of which imply that preliminary collapse (as a response to subsurface volume loss) resulted from flood discharge drainage into the subsurface prior to the onset of collapse. Drainage of subsequent floods directly into the forming depression likely led to further collapse. Some of the individual cavi (the peripheral cavi) display no surface inlets or outlets of water, indicating that lateral propagation of groundwater from the point of drainage led to subsurface volume loss at a distance from the surface floods. The direct association of the cavi and inflow channels makes non-water-mediated processes less likely. Furthermore, our morphologic analysis revealed no evidence of a volcanic or magmatic origin for the cavi. Structurally controlled topography and weakness planes associated with past stress fields appear to have influenced cavi formation, particularly by controlling the flow of water on the surface, into and within the subsurface. An origin of the cavi by aquifer breach, as suggested for some chaotic regions on Mars, cannot be excluded, though we note that no morphologic evidence for a catastrophic outlet of the water was observed on the surface in the region.

It is conceivable that some of the subsurface volume was lost by the release of ground volatiles and/or the physical transport of insoluble material through excavated subsurface fractures. However, it is highly unlikely that the entire missing volume down to ~ 2,800 m depth can be attributed solely to such mechanisms. We suggest instead that dissolution of buried salts by the infiltrating flood water accounts for most of the subsurface volume loss. Our regional mapping shows that the cavi occur on a Hesperian-age, low-relief surface, which we interpret as an ancient sedimentary basin. Valley networks regionally dissipate at this proposed basin, which may have been part of a larger body of water. The observations that the cavi specifically formed only when the outflow channels reached the basin, as well as the overlap of the cavi's western and southern boundaries with the basin boundaries, lead us to suggest that this sedimentary sequence may host subsurface evaporites. In the specific location of Osuga Cavi, these evaporites may have dissolved by interaction with the draining flood water. The estimated volume of water that formed the channels and the volume of dissolved salts that this water could carry highlight dissolution of subsurface magnesium sulfates as a possible explanation for most of the missing volume that caused the cavi collapse. Detections of thick sequences of layered deposits with spectral indications of magnesium sulfates are known from several adjacent regions[18–20]. Published ages of these deposits[1] are consistent with crater-counting model ages of ~ 3.6 Ga for the basin[58]. The plausibility of subsurface salt dissolution as a formation mechanism is further supported by analogy between the geomorphologically constrained order of events at Osuga and a previously studied terrestrial site at the Ze'elim alluvial fan near the Dead Sea. At the analog site, time-progressive subsurface salt dissolution by flood water drainage into sinkholes was documented as the main agent of pit growth and surface collapse.

Although the channel-cavi association observed at Osuga is special among Martian depressions, the formation of such depression by salt dissolution may not be unique to this site. Subsurface salt dissolution by undersaturated groundwater may have played a role in the formation of other Martian depressions, similar to sinkhole formation on Earth. Undersaturated groundwater could source from magmatism- or impact-driven dehydration of hydrated salts and clays[21]. Contact between preexisting undersaturated groundwater and the salts may also be facilitated by changes in salty groundwater levels (e.g., due to an adjacent sea level drop, confined aquifer breach, etc.) that cause a shift in the location of the interface between salty and fresher groundwater. The mapped channel-cavi association at Osuga Cavi serves to demonstrate that such mechanisms can explain the formation of some Martian depressions. Discovery of

other depressions on Mars that plausibly formed by salt dissolution may offer opportunities to constrain the spatial extent of buried salts. For example, such depressions in regions of insoluble volcanic or regolith cover that separates distant salt outcrops may support the subsurface continuity of the dissolution-susceptible units. More generally, our study showcases surface morphology as a powerful probe of subsurface stratigraphy and structure, offering unique constraints on planetary climate, hydrology and geochemistry.

Methods

Mapping was primarily based on a Mars Reconnaissance Orbiter Context Camera (CTX)[65] image mosaic rendered at 5 m per pixel (Fig. S1)[66]. We used elevations from Mars Express' High-Resolution Stereo Camera (HRSC) digital terrain models (DTMs) and anaglyphs[67, 68] to support morphological interpretations and Mars Odyssey's Thermal Emission Imaging System (THEMIS) thermal inertia image data (Fig. S1)[69] to support geologic interpretations. These different data types (e.g., CTX, elevation and THEMIS day and night IR) emphasize different surface attributes (Fig. S1) and the differences were used to help delineate the mapping units and their boundaries. We used High-Resolution Imaging Science Experiment (HiRISE) images[70] for detailed mapping and interpretation of small outcrops at specific locations. The mapped area (88,000 km^2; Figs. 1, 2) overlaps the − 15037 quadrangle (latitude 12.5° to 17.5° S., longitude 35° to 40° W.), except at its western boundaries where it closely follows the estimated watershed of the studied basin. We mapped geologic features at a scale between 1:50,000 and 1:100,000 and locally at a scale between 1:1,000 and 1:10,000. Surface features were mapped using ESRI's ArcMap® 10.6 software. At the boundaries of the mapped area, our units are consistent with those in neighboring maps of Margaritifer Terra[59, 60] and with relative terrain ages based on crater counting[58].

The volume of Osuga's channel system, chaotic terrains and terminal cavi were calculated in the ArcGIS® software using the Mars Global Surveyor's Mars Orbiter Laser Altimeter (MOLA) DTM (463 m per pixel resolution)[71]. We manually delineated the segment (channels, chaotic origins, cavi) boundaries using CTX images and curvature maps derived from the MOLA DTMs. We then generated a triangular-irregular network-based raster[72]. The raster linearly interpolates elevation from the surrounding surface across the segment boundaries, effectively producing a cap that represents the preexisting (i.e., pre chaos formation, pre channel incision, pre cavi collapse) surface (Fig. S4). A similar approach was adopted in previous studies[73, 74]. The spatial resolution of the CTX images, in which the chaos, channel and cavi boundaries were identified, is higher than the MOLA DTMs used to constrain the elevation at the rims of these features. This results in artifactually low elevation due to averaging of true elevations on either side of the feature boundaries. To avoid such artifacts, the preexisting surface was interpolated between points located 1,150 m outward from the boundaries identified in the CTX images. We found that this distance is sufficient to avoid elevation artifacts while remaining representative of the boundaries' true location. We calculated the elevation difference between the MOLA DTM and the interpolated preexisting surface and summed these elevation differences multiplied by the pixel area to calculate the missing volume. Volumes calculated this way are an approximate estimate of subsurface volume loss (see Results and Discussion), with uncertainty associated with the manual choice of segment boundaries, errors in horizontal and vertical location (~ 100 m and ~ 3 m, respectively)[75], and artifacts of the interpolation to generate the pre-outflow surface[73].

The channel volume serves as a lower bound on the integrated volume of sediment carried by the floods (V_{sed}), since sediments from the chaotic flood origin region and sediment deposition within the channels are not accounted for. Assuming that most of this sediment was transported by near-peak discharge, which corresponds also to near-peak sediment load, this lower bound on the transported sediment may be turned into a conservatively low estimate of the volume of water that carried this sediment. Though maximal sediment loads are suggested to be ~ 40% (ref. 76), the morphology of the channels is more consistent with lower-viscosity fluids, and we adopt a range of sediment load

between 5 and 20%. The volume of water is then calculated as $V_{water} = V_{sed}(1/f_{sed} - 1)$, where f_{sed} is the volume fraction of sediment in the flood[77].

With the volume of water calculated as described above, we calculated the maximal volume of salts that this estimated volume of water could have dissolved if it drained into the cavi's subsurface. We assumed that the water reached saturation with the buried salts of interest prior to leaving the system, which is equivalent to an assumption of sufficiently long residence times of the water in contact with the salts. This assumption seems reasonable given typically low rates of water flow in most subsurface conduits. In the salt volume calculations, we included mineral families detected on Mars or in Martian meteorites[78], considering a wide range of salts within those families. These include calcium sulfates (gypsum, bassanite, anhydrite), magnesium sulfates (epsomite, hexahydrite, pentahydrite, starkeyite, kieserite), iron sulfates (potassium/sodium/hydronium-jarosite), alunite, calcium carbonates (calcite, aragonite), magnesium and ferroan carbonates (dolomite, magnesite, siderite), chlorides (halite, sylvite, bischofite), and perchlorates ($NaClO_4 \times H_2O$, $NaClO_4 \times 2H_2O$, $KClO_4$, $Mg(ClO_4)_2 \times 6H_2O$, $Mg(ClO_4)_2 \times 8H_2O$, $Ca(ClO_4)_2 \times 6H_2O$). Most mineral solubility constants were taken from the Lawrence Livermore National Laboratory (LLNL) Thermodynamic Database[79], to which a variety of sulfate and chloride mineral data were added in a previous study[80]. For consistency, the first and second acid dissociation constants used in the calculations of the carbonate mineral volumes were taken from the LLNL database. The mineral solubility constants of the perchlorate minerals were taken from a previous study[81]. Since the temperature dependence of the solubility of many of the minerals of interest here is unknown, we used the solubility constants at 25°C (Table S1) and note that this may result in a slight overestimate of the amounts of sulfate, chloride and perchlorate salts dissolved, and a slight underestimate of the amounts of carbonate minerals dissolved. The uncertainty associated with this choice and with the assumption of solution saturation is small relative to the uncertainty associated with estimation of the water volume.

Declarations

Competing Interests

The authors declare no competing interests.

Author Contributions

R.N. designed the work and carried out the analysis under the supervision of V.C.G., I.H., and A.M. All authors contributed to the interpretation of the results and jointly wrote the manuscript.

Acknowledgements

We thank O. Aharonson, I. Haviv, A. Hayes, M. Abelson, G. Baer, H.I. Hargitai, N.H. Glines, and R. Nativ for fruitful discussions and suggestions. We are grateful to C.M. Weitz and S.H. Purdy for sharing their pre-publication mapping of quadrangles adjacent to the study site. We acknowledge the work of D. Portillo, and R. Spurling on additional aspects of this study site that indirectly contributed to our understanding of the site's history. We highlight the contribution of O. Hetzroni who produced Fig. 7. R.N. acknowledges an Assaf Ramon Fellowship from the Israeli Space Agency, which funded participation in the International Intern (I^2) program at NASA Ames Research Center, under the mentorship of V.C.G. V.C.G. was funded by NAI grant # NNX15BB01 and MRO-HiRISE Co-Investigator funds. I.H. acknowledges funding from the Helen Kimmel Center for Planetary Sciences at the Weizmann Institute of Science.

Data Availability

The data presented in the paper and in the Supplementary Information is sufficient to evaluate the conclusions in the paper. Additional data related to this paper may be requested from the authors.

The HiRISE data were retrieved from https://www.uahirise.org/. The global CTX mosaic was retrieved from https://murray-lab.caltech.edu/CTX/. The global THEMIS mosaics were retrieved from https://astrogeology.usgs.gov/search/map/Mars/Odyssey/THEMIS-IR-Mosaic ASU/Mars_MO_THEMIS-IR-Day_mosaic_global_100m_v12 and https://astrogeology.usgs.gov/search/map/Mars/Odyssey/THEMIS-IR-Mosaic-ASU/Mars_MO_THEMIS-IR-Night_mosaic_60N60S_100m_v14. The HRSC data were shared by D. Tirsch. The global MOLA DEM was retrieved from https://astrogeology.usgs.gov/search/map/Mars/GlobalSurveyor/MOLA/Mars_MGS_MOLA_DEM_mosaic_global_463m.

References

1. Bibring, J.P. et al., 2006, Global mineralogical and aqueous Mars history derived from OMEGA/Mars express data: Science, v. 312, p. 400–404, doi:10.1126/science.1122659.
2. Grotzinger, J.P., and Milliken, R.E., 2012, The sedimentary record of Mars: Distribution, origins and global stratigraphy: Sedimentary Geology of Mars, Grotzinger, J.P., and Milliken, R.E. Eds., SEPM Society for Sedimentary Geology, doi: 10.2110/pec.12.102.0001.
3. Ehlmann, B.L., et al., 2016, The sustainability of habitability on terrestrial planets: Insights, questions, and needed measurements from Mars for understanding the evolution of Earth-like worlds: Journal of Geophysical Research, v. 121, p. 1927–1961.
4. Shviro, M., Haviv, I., and Baer, G., 2017, High-resolution InSAR constraints on flood-related subsidence and evaporite dissolution along the Dead Sea shores: Interplay between hydrology and rheology: Geomorphology, v. 293, p. 53–68, doi:10.1016/j.geomorph.2017.04.033.
5. Whitten, J.L., and Martin, E.S., 2019, Icelandic pit chains as planetary analogs: Using morphologic measurements of pit chains to determine regolith thickness: Journal of Geophysical Research, v. 124, p. 2983–2999.
6. Naor, R., Mushkin, A., and Halevy, I., 2023, Morphometric constraints on the formation of new terrestrial analogs for planetary pits: Geological Society of America Bulletin, v. 135, 2200–2218.
7. Sharp, R.P., 1973, Mars: South polar pits and etched terrain: Journal of Geophysical Research, v. 78, p. 4222–4230.
8. Tanaka, K.I., and Golombek, M.P., 1989, Martian tension fractures and the formation of grabens and collapse features at Valles Marineris: Proceedings of the 19th Lunar and Planetary Science Conference, p. 383–396.
9. Jackson, M.P.A., Adams, J.B., Dooley, T.P., Gillespie, A.R., and Montgomery, D.R., 2011, Modeling the collapse of Hebes Chasma, Valles Marineris, Mars: Geological Society of America Bulletin, v. 123, p. 1596–1627, doi:10.1130/B30369.1.
10. Graettinger, A.H., and Hughes, C.G., 2019, Maar recognition on Mars based on a list of morphologic criteria, with one remaining limitation of secondary craters: Proceedings of the 50th Lunar and Planetary Science Conference, No. 2132, ID 1254.
11. Broz, P., Bernhardt, H., Conway, S.J., and Parekh, R., 2021, An overview of explosive volcanism on Mars: Journal of Volcanology and Geothermal Research, v. 409, 107125.
12. Wyrick, D., Ferrill, D.A., Morris, A.P., Colton, S.L., and Sims, D.W., 2004, Distribution, morphology, and origins of Martian pit crater chains: Journal of Geophysical Research, v. 109, E06005.
13. Schaefer, M.W., 1990, Karst on Mars? The thumbprint terrain: Icarus, v. 83, p. 244–247, doi:10.1016/0019-1035(90)90017-4.

14. Spencer, J.R., and Fanale, F.P., 1990, New models for the origin of Valles Marineris closed depressions: Journal of Geophysical Research, v. 95, p. 14301–14313, doi:10.1029/JB095iB09p14301.
15. Rodriguez, J.A.P., Kargel, J.S., Tanaka, K.L., Crown, D.A., Berman, D.C., Fairén, A.G., Baker, V.R., Furfaro, R., Candelaria, P., and Sasaki, S., 2011, Secondary chaotic terrain formation in the higher outflow channels of southern circum-Chryse, Mars: Icarus, v. 213, p. 150–194, doi:10.1016/j.icarus.2010.09.027.
16. Osterloo, M.M. et al., 2008, Chloride-bearing materials in the Southern Highlands of Mars: Science, v. 319, p. 1651–1654.
17. Bridges, J.C., Hicks, L.J., and Treiman, A.H., 2019, Carbonates on mars: Elsevier Inc., v. 5, 89–118 p., doi:10.1016/B978-0-12-804191-8.00005-2.
18. Arvidson, R.E., Poulet, F., Bibring, J.P., Wolff, M., Gendrin, A., Morris, R. V., Freeman, J.J., Langevin, Y., Mangold, N., and Bellucci, G., 2005, Spectral reflectance and morphologic correlations in eastern Terra Meridiani, Mars: Science, v. 307, p. 1591–1594, doi:10.1126/SCIENCE.1109509.
19. Langevin, Y., Poulet, F., Bibring, J.P., and Gondet, B., 2005, Sulfates in the north polar region of Mars detected by OMEGA/Mars express: Science, v. 307, p. 1584–1586, doi:10.1126/SCIENCE.1109091.
20. Gendrin, A., Mangold, N., Bibring, J., Langevin, Y., Gondet, B., Bonello, G., Quantin, C., Mustard, J., and Arvidson, R., 2005, Sulfates in Martian Layered Terrains: The OMEGA / Mars Express View: v. 307, p. 1587–1592.
21. Montgomery, D.R., and Gillespie, A., 2005, Formation of Martian outflow channels by catastrophic dewatering of evaporite deposits: Geology, v. 33, p. 625–628, doi:10.1130/G21270.1.
22. Flahaut, J., Quantin, C., Allemand, P., Thomas, P., and Le Deit, L., 2010, Identification, distribution and possible origins of sulfates in Capri Chasma (Mars), inferred from CRISM data: Journal of Geophysical Research: Planets, v. 115, p. 1–10, doi:10.1029/2009JE003566.
23. Adams, J.B., Gillespie, a. R., Jackson, M.P. a., Montgomery, D.R., Dooley, T.P., Combe, J.P., and Schreiber, B.C., 2009, Salt tectonics and collapse of Hebes Chasma, Valles Marineris, Mars: Geology, v. 37, p. 691–694, doi:10.1130/G30024A.1.
24. Sholes, S.F., Dickeson, Z.I., Montgomery, D.R., and Catling, D.C., 2021, Where are Mars' hypothesized ocean shorelines? Large lateral and topographic offsets between different versions of paleoshoreline maps: Journal of Geophysical Research: Planets, v. 126, p. E2020JE006486, doi: https://doi.org/10.1029/2020JE006486.
25. De Toffoli, B., Plesa, A.-C., Hauber, E., and Breuer, D., 2021, Delta deposits on Mars: A global perspective. Geophysical Research Letters, v. 48, p. e2021GL094271, doi: https://doi.org/10.1029/2021GL094271.
26. Baker, V.R., Strom, R.G., Gulick, V.C., Kargel, J.S., Komatsu, G., and Kale, V.S., 1991, Ancient oceans, ice sheets and the hydrological cycle on Mars: Nature, v. 352, p. 589–594, doi:10.1038/352589a0.
27. Rodriguez, J.A.P. et al., 2015a, Martian outflow channels: How did their source aquifers form, and why did they drain so rapidly? Scientific Reports, v. 5, p. 13404, doi:10.1038/srep13404.
28. Parker, T., and Bills, B., 2021, Mars Northern Plains Ocean: Elsevier Inc., 41–59 p., doi:10.1130/abs/2020am-359127.
29. Bishop, J.L., Yeşilbaş, M., Hinman, N.W., Burton, Z.F.M., Englert, P.A.J., Toner, J.D., McEwen, A.S., Gulick, V.C., Gibson, E.K., and Koeberl, C., 2021, Martian subsurface cryosalt expansion and collapse as trigger for landslides: Science Advances, v. 7, p. 1–14, doi:10.1126/sciadv.abe4459.
30. Sarkar, R., Edgett, K.S., Singh, P., and Porwal, A., 2018, The light-toned stratified sedimentary rock exposures in western Juventae Chasma, Mars, in context: Icarus, v. 312, p. 7–35, doi:10.1016/j.icarus.2018.04.010.
31. Rodriguez, J.A.P. et al., 2012, Infiltration of Martian outflow channel floodwaters into lowland cavernous systems: Geophysical Research Letters, v. 39, p. 1–7, doi:10.1029/2012GL053225.
32. Baioni, D., and Wezel, F.C., 2010, Morphology and origin of an evaporitic dome in the eastern Tithonium Chasma, Mars: Planetary and Space Science, v. 58, p. 847–857, doi:10.1016/j.pss.2010.01.009.

33. Baioni, D., Zupan Hajna, N., and Wezzel, F.C., 2011, Karst landforms in an interior layered deposit within the Coprates Chasma, Mars: Acta Carsologica, v. 40, p. 473–481, doi:10.3986/AC.V40I3.59.
34. Baioni, D., and Sgavetti, M., 2013, Karst terrains as possible lithologic and stratigraphic markers in northern Sinus Meridiani, Mars: Planetary and Space Science, v. 75, p. 173–181, doi:10.1016/j.pss.2012.08.011.
35. Baioni, D., and Tramontana, M., 2015, Evaporite karst in three interior layered deposits in Iani Chaos, Mars: Geomorphology, v. 245, p. 15–22, doi:10.1016/j.geomorph.2015.05.018.
36. Baioni, D., and Tramontana, M., 2017, Possible evaporite karst in an interior layered deposit in Juventae Chasma, Mars: Mars. International Journal of Speleology, v. 46, p. 181–189, doi:10.5038/1827-806X.46.2.2085.
37. Boothroyd, J.C., 1982, Ancient fluvial drainage systems: Margaritifer Sinus area, Mars, *in* Reports of Planetary Geology Program, NASA Tech. Memo. 85127, p. 209–212.
38. Baker, V.R., 2001, Water and the martian landscape: Nature, v. 412, p. 228–236, doi:10.1038/35084172.
39. Schultz, P.H., Schultz, R.A., and Rogers, J., 1982, The structure and evolution of ancient impact basins on Mars: Journal of Geophysical Research, v. 87, p. 9803, doi:10.1029/jb087ib12p09803.
40. Grant, G.A., 1987, The geomorphic evolution of Eastern Margaritifer Sinus, Mars, in Advances in Planetary Geology, NASA Technical Memorandum 89871, 1–268.:
41. Schultz, R.A., and Frey, H. V., 1990, A new survey of multiring impact basins on Mars: Journal of Geophysical Research, v. 95, doi:10.1029/jb095ib09p14175.
42. Cartwright, S.F.A., and Seelos, K.D., 2019, New Ring Structure Estimates of Ladon Basin, Mars, from Mafic Mineral Mapping with CRISM: 50th Annual Lunar and Planetary Science Conference, 2019, No. 2132, p. 2.
43. Parker, T.J., and Pieri, D.C., 1985, Geomorphology and geology of the southwestern Margaritifer Sinus and Argyre regions of Mars-I: Geological and geomorphological overview, *in* Holt, H.E. and Watters, T.R. eds., Reports of Planetary Geology and Geophysics Program, NASA Tech. Memo. 87563, p. 361–363.
44. Avni, Y. et al., 2016, Self-accelerated development of salt karst during flash floods along the Dead Sea Coast, Israel: Journal of Geophysical Research: Earth Surface, v. 121, p. 17–38, doi:10.1002/2015JF003738.
45. Abelson, M., Baer, G., Shtivelman, V., Wachs, D., Raz, E., Crouvi, O., Kurzon, I., and Yechieli, Y., 2003, Collapse-sinkholes and radar interferometry reveal neotectonics concealed within the Dead Sea basin: Geophysical Research Letters, v. 30 (10), p. 1545, doi:10.1029/2003GL017103.
46. Shalev, E., and Lyakhovsky, V., 2012, Viscoelastic damage modeling of sinkhole formation: Journal of Structural Geology, v. 42, p. 163–170, doi:10.1016/j.jsg.2012.05.010.
47. Atzori, S., Antonioli, A., Salvi, S., and Baer, G., 2015, InSAR-based modeling and analysis of sinkholes along the Dead Sea coastline: Geophysical Research Letters, v. 42, p. 8383–8390, doi:10.1002/2015GL066053.
48. Arav, R., Filin, S., and Avni, Y., 2020, Sinkhole swarms from initiation to stabilisation based on in situ high-resolution 3-D observations: Geomorphology, v. 351, doi:10.1016/j.geomorph.2019.106916.
49. Baer, G., Swaed, I., Nof, R., Bernstein, M., and Gavrieli, I., 2021, Recharge and discharge of floodwater in sinkholes along the Dead Sea: implications for long-term geomorphological changes: Israel Geological Society | Yeruham |2021, p. 1–105, doi:10.1109/iccceee49695.2021.9429649.
50. Bishop, J.L. et al., 2009, Mineralogy of Juventae Chasma: Sulfates in the light-toned mounds, mafic minerals in the bedrock, and hydrated silica and hydroxylated ferric sulfate on the plateau: Journal of Geophysical Research, v. 114, p. E00D09, doi:10.1029/2009JE003352.
51. Fueten, F., Flahaut, J., Le Deit, L., Stesky, R., Hauber, E., and Gwinner, K., 2011, Interior layered deposits within a perched basin, southern Coprates Chasma, Mars: Evidence for their formation, alteration, and erosion: Journal of Geophysical Research: Planets, v. 116, p. 1–18, doi:10.1029/2010JE003695.

52. Kleinhans, M.G., 2005, Flow discharge and sediment transport models for estimating a minimum timescale of hydrological activity and channel and delta formation on Mars: Journal of Geophysical Research E: Planets, v. 110, p. 1–23, doi:10.1029/2005JE002521.
53. Robbins, S.J., Hynek, B.M., Lillis, R.J., and Bottke, W.F., 2013, Large impact crater histories of Mars: The effect of different model crater age techniques: Icarus, v. 225, p. 173–184, doi:10.1016/j.icarus.2013.03.019.
54. Niles, P.B., Catling, D.C., Berger, G., Chassefière, E., Ehlmann, B.L., Michalski, J.R., Morris, R., Ruff, S.W., and Sutter, B., 2013, Geochemistry of carbonates on Mars: Implications for climate history and nature of aqueous environments: Space Science Reviews, v. 174, p. 301–328, doi:10.1007/s11214-012-9940-y.
55. Glotch, T.D., and Rogers, A.D., 2007, Evidence for aqueous deposition of hematite- and sulfate-rich light-toned layered deposits in Aureum and Iani Chaos, Mars: Journal of Geophysical Research: Planets, v. 112, p. 1–11, doi:10.1029/2006JE002863.
56. Gaillard, F., Michalski, J., Berger, G., McLennan, S.M., and Scaillet, B., 2013, Geochemical reservoirs and timing of sulfur cycling on Mars: Space Science Reviews, v. 174, p. 251–300, doi:10.1007/s11214-012-9947-4.
57. Sowe, M., Jaumann, R., and Neukum, G., 2011, A comparative study of interior layered deposits on Mars: Geological Society Special Publication, v. 356, p. 281–300, doi:10.1144/SP356.14.
58. Spurling, R., Gulick, V.C., and Naor, R., 2023, 54th Lunar and Planetary Science Conference 2023 (LPI Contrib. No. 2806) 2895.pdf: v. 2023, p. 4–5.
59. Wilson, S.A., and Grant, J.A. (in revision), Geologic Map of MTM quadrangles – 20037, -25037, -30037, and – 30032, Northwestern Noachis Terra Region of Mars:
60. Weitz, C.M., Wilson, S.A., Grant, J.A., and Irwin III, R.P. (in press.), Geologic Map of Western Ladon basin, Mars:
61. Robbins, S.J., Hynek, B.M., Lillis, R.J., and Bottke, W.F., 2013, Large impact crater histories of Mars: The effect of different model crater age techniques: Icarus, v. 225, p. 173–184, doi:10.1016/j.icarus.2013.03.019.
62. Milliken, R.E., Fischer, W.W., and Hurowitz, J. a., 2009, Missing salts on early Mars: Geophysical Research Letters, v. 36, p. 1–5, doi:10.1029/2009GL038558.
63. Halevy, I., and Head III, J.W., 2014, Episodic warming of early Mars by punctuated volcanism: Nature Geoscience, v. 7, p. 865–868, doi:10.1038/ngeo2293.
64. Rodriguez, J.A.P., Platz, T., Gulick, V., Baker, V.R., Fairén, A.G., Kargel, J., Yan, J., Miyamoto, H., and Glines, N., 2015b, Did the martian outflow channels mostly form during the Amazonian Period? Icarus, v. 257, p. 387–395, doi:10.1016/J.ICARUS.2015.04.024.
65. Malin, M.C. et al., 2007, Context Camera Investigation on board the Mars Reconnaissance Orbiter: Journal of Geophysical Research: Planets, v. 112, p. 1–25, doi:10.1029/2006JE002808.
66. Dickson, J.L., Kerber, L.A., Fassett, C.I., and Ehlmann, B.L., 2018, A global, blended CTX mosaic of Mars with vectorized seam mapping: A new mosaicking pipeline using principles of non-destructive image editing: 49th Lunar and Planetary Science Conference, The Woodlands, Texas, USA, Lunar and Planetary Institute, no. 2083, p. 2.
67. Neukum, G., and Jaumann, R., 2004, HRSC: the High Resolution Stereo Camera of Mars Express, *in* Mars express: The Scientific Payload, p. 17–35.
68. Jaumann, R. et al., 2007, The high-resolution stereo camera (HRSC) experiment on Mars Express: Instrument aspects and experiment conduct from interplanetary cruise through the nominal mission: Planetary and Space Science, v. 55, p. 928–952, doi:10.1016/j.pss.2006.12.003.
69. Christensen, P.R. et al., 2004, The thermal emission imaging system (THEMIS) for the Mars 2001 Odyssey Mission: Space Science Reviews, v. 110, p. 85–130.
70. McEwen, A.S. et al., 2007, Mars Reconnaissance Orbiter's High Resolution Imaging Science Experiment (HiRISE): Journal of Geophysical Research, v. 112, p. E05S02, doi:10.1029/2005JE002605.

71. Smith, D.E. et al., 2001, Mars Orbiter Laser Altimeter: Experiment summary after the first year of global mapping of Mars: Journal of Geophysical Research: Planets, v. 106, p. 23689–23722, doi:10.1029/2000JE001364.
72. Cooley, S., 2015, GIS 4 Geomorphology:, p. 1–16, https://docs.wixstatic.com/ugd/13658e_26aa5728add84d9da3dbc4f8cc4fc39d.pdf.
73. Noreen, E., and Hare, T.M., 2002, Volumetric Calculations of Valles Marineris Using MOLA Data and GIS:, p. 4–5.
74. Gulick, V.C., Glines, N., Hart, S., and Freeman, P., 2018, Geomorphological analysis of gullies on the central peak of Lyot Crater, Mars: Geological Society, London, Special Publications, v. 467, p. 233–265, doi:10.1144/sp467.17.
75. Neumann, G.A., Rowlands, D.D., Lemoine, F.G., Smith, D.E., and Zuber, M.T., 2001, Crossover analysis of Mars Orbiter Laser Altimeter data: Journal of Geophysical Research: Planets, v. 106, p. 23753–23768, doi:10.1029/2000JE001381.
76. Komar, P.D., 1980, Modes of sediment transport in channelized water flows with ramifications to the erosion of the Martian outflow channels: Icarus, v. 42, p. 317–329, doi:10.1016/0019-1035(80)90097-4.
77. Leask, H.J., Wilson, L., and Mitchell, K.L., 2007, Formation of Mangala Valles outflow channel, Mars: Morphological development and water discharge and duration estimates: Journal of Geophysical Research: Planets, v. 112, p. 1–12, doi:10.1029/2006JE002851.
78. Ehlmann, B.L., and Edwards, C.S., 2014, Mineralogy of the Martian surface: Annual Review of Earth and Planetary Sciences, v. 42, p. 291–315, doi:10.1146/annurev-earth-060313-055024.
79. Johnson, J., Anderson, F., and Parkhurst, D.L., 2000, Database Thermo.com.V8.R6.230e, Lawrence Livermore National Laboratory, Livermore, CA, USA:
80. Tosca, N.J., McLennan, S.M., Clark, B.C., Grotzinger, J.P., Hurowitz, J. a., Knoll, a. H., Schröder, C., and Squyres, S.W., 2005, Geochemical modeling of evaporation processes on Mars: Insight from the sedimentary record at Meridiani Planum: Earth and Planetary Science Letters, v. 240, p. 122–148, doi:10.1016/j.epsl.2005.09.042.
81. Marion, G.M., Catling, D.C., Zahnle, K.J., and Claire, M.W., 2010, Modeling aqueous perchlorate chemistries with applications to Mars: Icarus, v. 207, p. 675–685, doi:10.1016/j.icarus.2009.12.003.

Figures

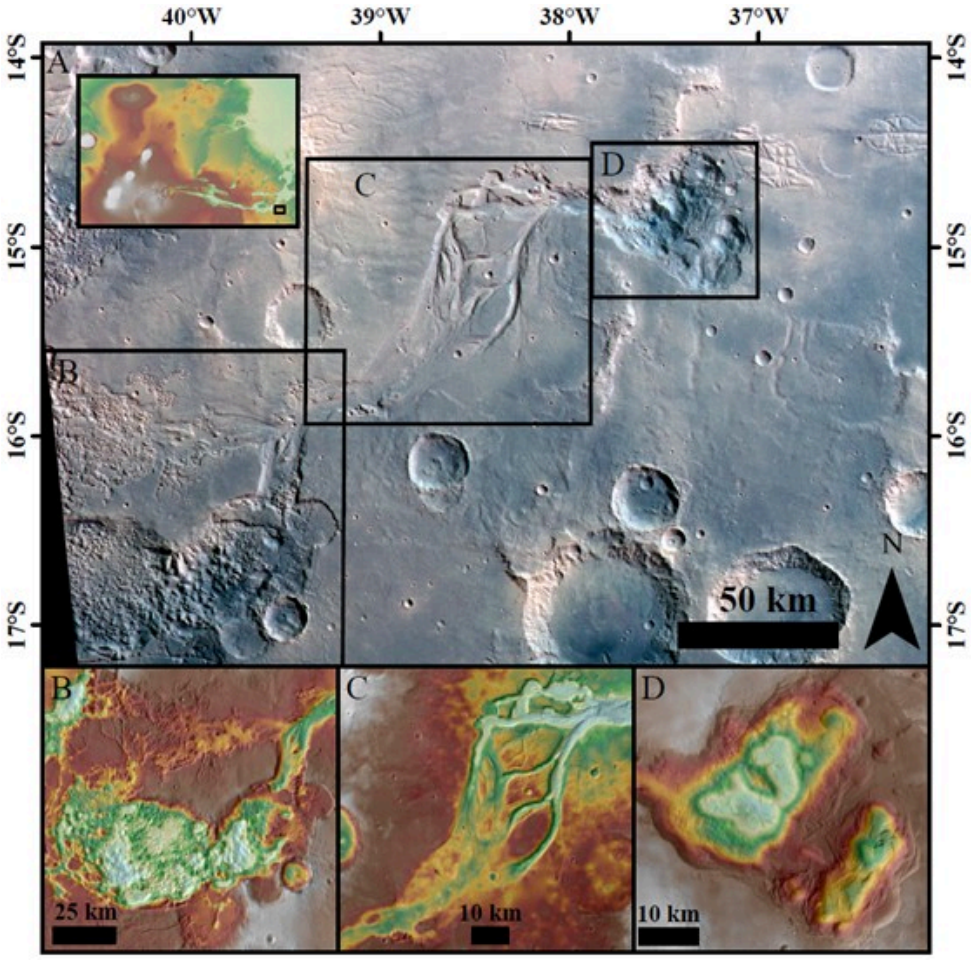

Figure 1

Osuga Valles. (A) A false-color image of the Osuga Valles system (from HRSC image H0533_IHS). Black boxes outline the locations of panels B-D. See inset at the upper left for location on Mars (elevation range –5,900 to +21,000 m) (B) The chaotic terrains at the system's origin (THEMIS Day IR with MOLA DTM, elevation range –800 to +1,700 m). (C) The Osuga outflow channels (CTX mosaic with HRSC H0533DA4 DTM, elevation range –1,100 to +1,500 m). (D) The Osuga terminal cavi (CTX mosaic with HRSC H0533DA4 DTM, elevation range –2,800 to +700 m). In panels B-D, warm and cool colors denote high and low elevations, respectively.

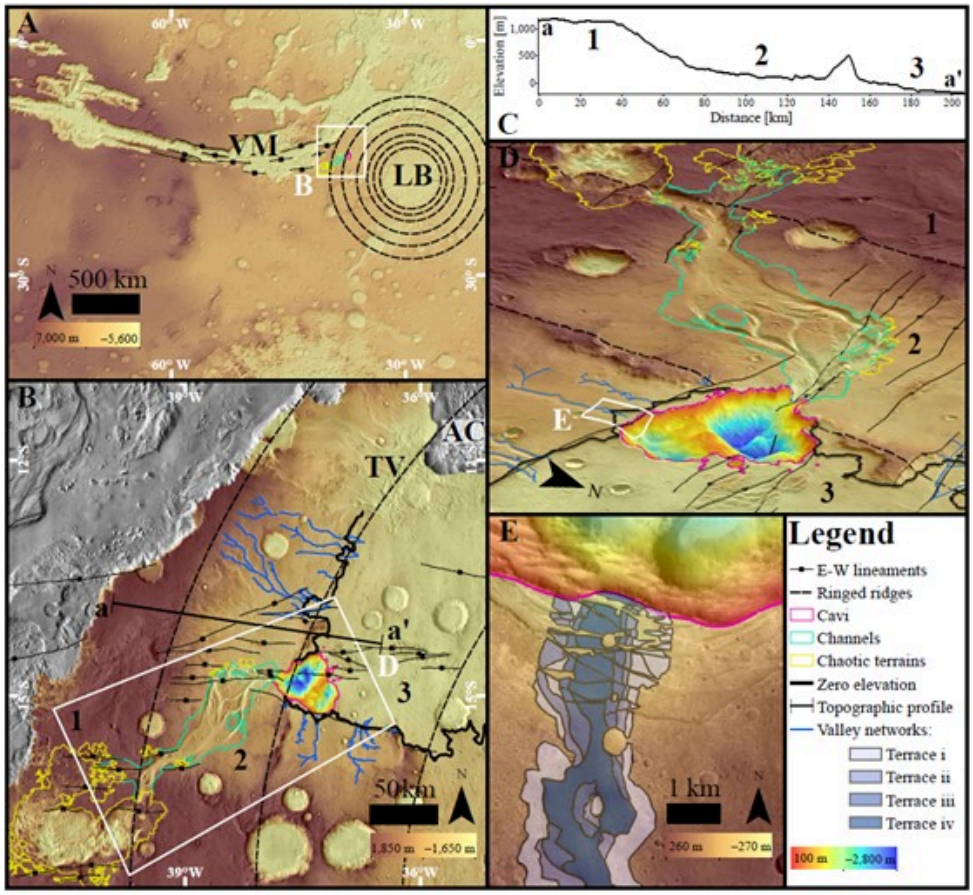

Figure 2

Study site and geologic setting. (A) Two regional geologic structures overlap in the study site: LB denotes the proposed ringed-ridge remnants of Ladon Basin, and VM denote the proposed extended fracture and fault system of Valles Marineris. Background is MOLA hill-shaded DTM. (B) The effect of the regional geologic structures at the study site. Numbers 1, 2 and 3 mark three distinct topographic stairs in panels B, C and D. Valley networks that dissipate at the basin on the lower stair are delineated. The thick black line is the zero-elevation contour, which closely follows the boundaries of the lower basin, here proposed to be an ancient sedimentary basin (unmarked at Osuga and Tigre Valles due to local destruction in those regions). Background is MOLA DTM overlying THEMIS Day IR. The color bar for the area enclosed within the cavi is in the legend. TV: chaotic terrain at the termini of Tigre Valles. AC: collapse and surface destruction extending south from Aurorae Chaos. (C) A MOLA-based elevation profile (~25 times vertically exaggerated) across the three topographic stairs (profile track is shown in panel B). (D) A perspective view of Osuga's three segments and their transition through LB ringed ridges along VM-associated features. Background is MOLA DTM overlying THEMIS Day IR with elevation color-coded as in panel B, three times vertically exaggerated. (E) A morphological map of a valley network channel that is cut by Osuga Cavi. Background is CTX underlying HRSC DTM.

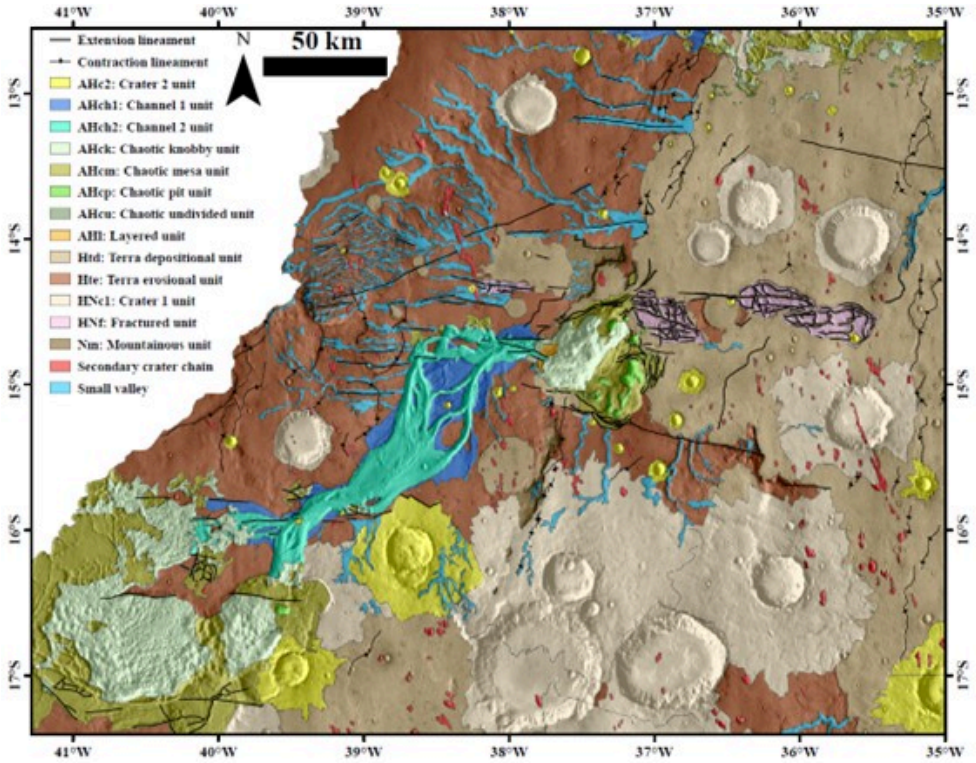

Figure 3

Geologic map of Osuga Valles' region. Unmapped areas are terrains beyond the lower stair's drainage basin.

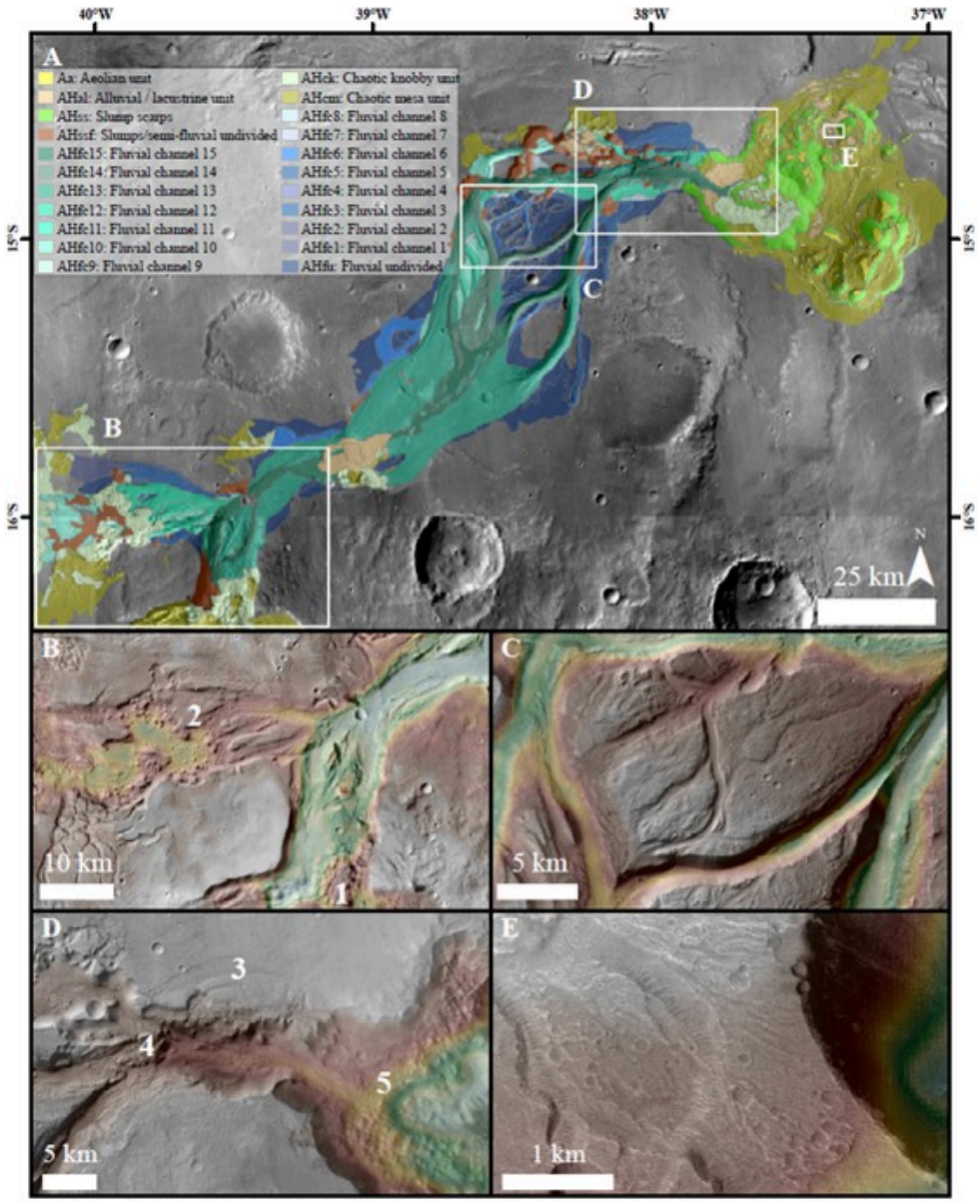

Figure 4

Morphology and topography of flood-related features. (A) Morphological map of color-coded flood events. Fluvial units are numbered 1-15 from old to young with 15 being the youngest flow. The background is a CTX mosaic. In panels B-D the CTX images are overlain by HRSC DTMs. (B) Two separate chaotic terrains at the system's head (elevation range 0 to +1,300 m). The association implies that the larger channel sourced from the southern chaotic terrain (label 1) postdates the outflow from the western chaotic terrain (label 2). (C) Smaller channels are cut by larger channels, suggesting higher-discharge outflow events that postdate earlier, lower-discharge events (elevation range –500 to +400 m). (D) Shallow channels on the upper plateau (label 3) are disconnected from the cavi (elevation range –2,700 to +300 m). The larger channels merge in a cataract (label 4). The merged channel downcuts the primary cavus floor but is cut by the internal nested cavus (label 5). (E) Fluvial morphologies are observed on top of remnant collapsed blocks within the cavi (elevation range –1,500 to –900 m). They are interpreted to be parts of an alluvial fan that may be associated with the sinusoidal upper channels that seem to predate the collapse.

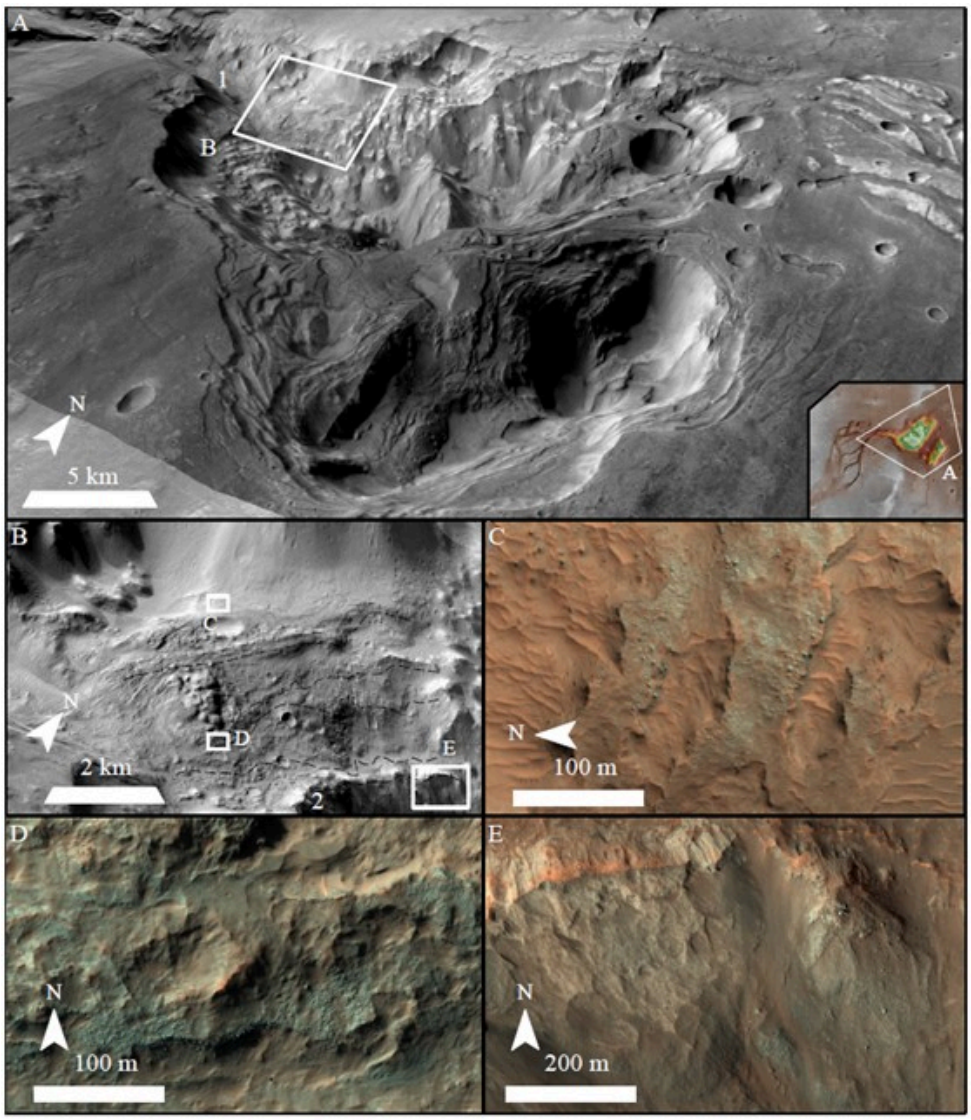

Figure 5

Stratified outcrops in Osuga's primary cavus. (A) Perspective view of Osuga Cavi. See inset at bottom right for elevations (elevation range –2,800 to +1,900 m). The terminal merged channel morphology outlet (label 1) continues inside the primary cavus. (B) Perspective view of intact terrain that superposes the bottom of the primary cavus and differs from the otherwise chaotic ruptured morphology of Osuga Cavi. Dashed lines delineate what appears as topographic benches (layers?). The merged channel on the bottom of the primary cavus (label 2) cuts the intact terrain but terminates at the rim of the internal nested cavus (label 5 in Fig. 4D). Panels A and B are CTX images draped on MOLA DTM (×3 vertical exaggeration) (Google Earth, NASA/USGS/ESA/DLR/FU Berlin (G. Neukum)). (C) An outcrop at the top of the intact terrain showing a boulder-like texture. (D) An outcrop at the center of the intact terrain showing an additional boulder-like texture. Panels C and D are from HiRISE image ESP_027880_1650. (E) An outcrop at the primary cavus floor (i.e., the rim of the nested cavus) showing a light-toned crust-like texture overlying a boulder-like texture. Taken from HiRISE image ESP_066583_1650.

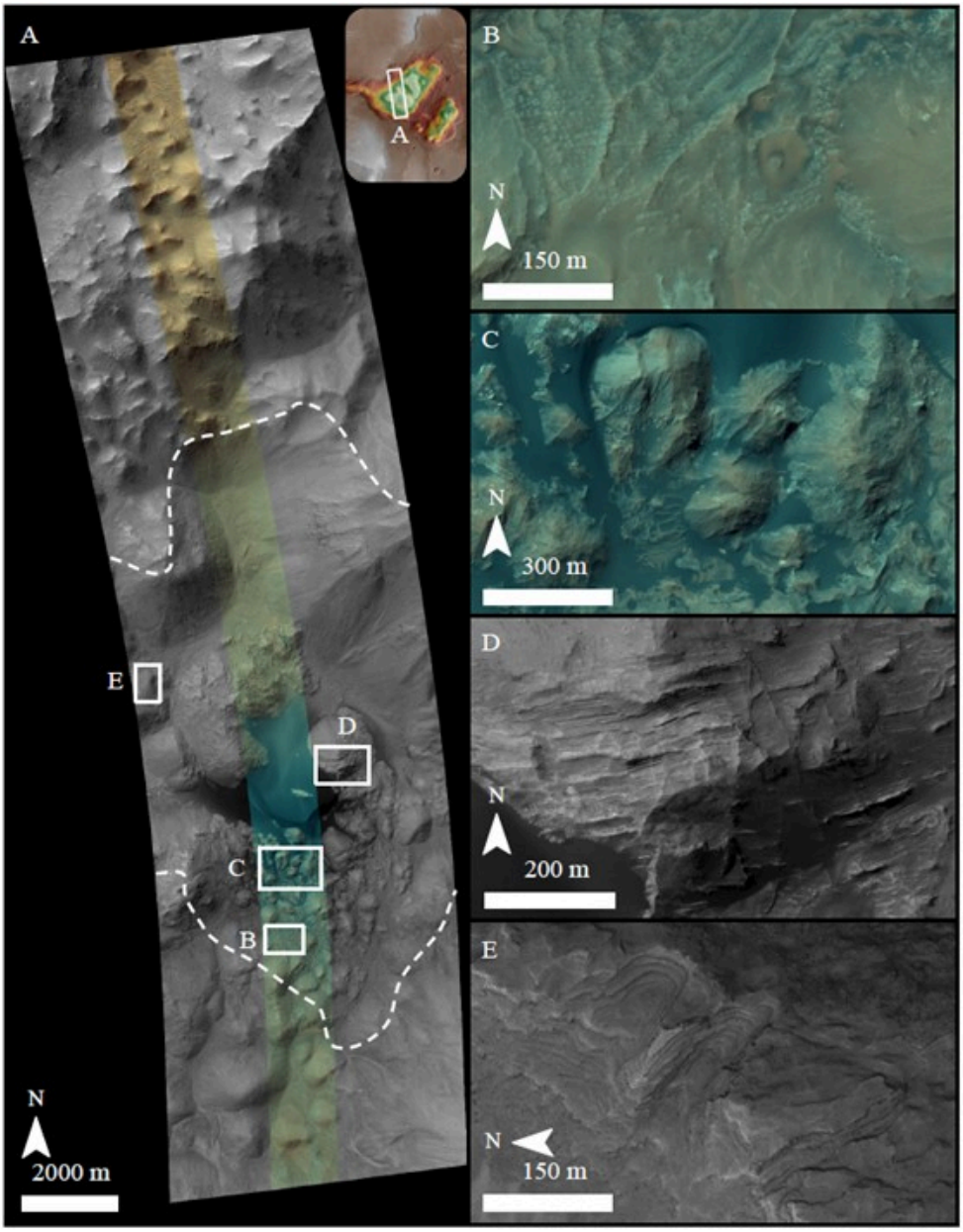

Figure 6

Sedimentary outcrops at the bottom of Osuga's internal secondary cavus. (A) A HiRISE image (ESP_060174_1650) transecting NNW-SSE along Osuga Cavi's primary and nested cavi. The walls and floor of the primary cavus are at the top and bottom of the image, respectively. The nested cavus, also seen in panels B-E, is at the center of the image and its approximate boundaries are delineated by the white dashed line. See inset for elevations (elevation range −2,800 to +900 m). (B) A polygonal surface underlying a massive (at HiRISE resolution) unit near the primary-nested cavi transition. (C) Blocks near the bottom of the nested cavus display discontinuous units overlain by dark eolian deposits. (D) A rise at the nested cavus' bottom displays E-W sub-horizontal finely bedded layering that is cut by a conjugated set of generally N-S positive relief lineaments. (E) Layers outcrop from a tilted block.

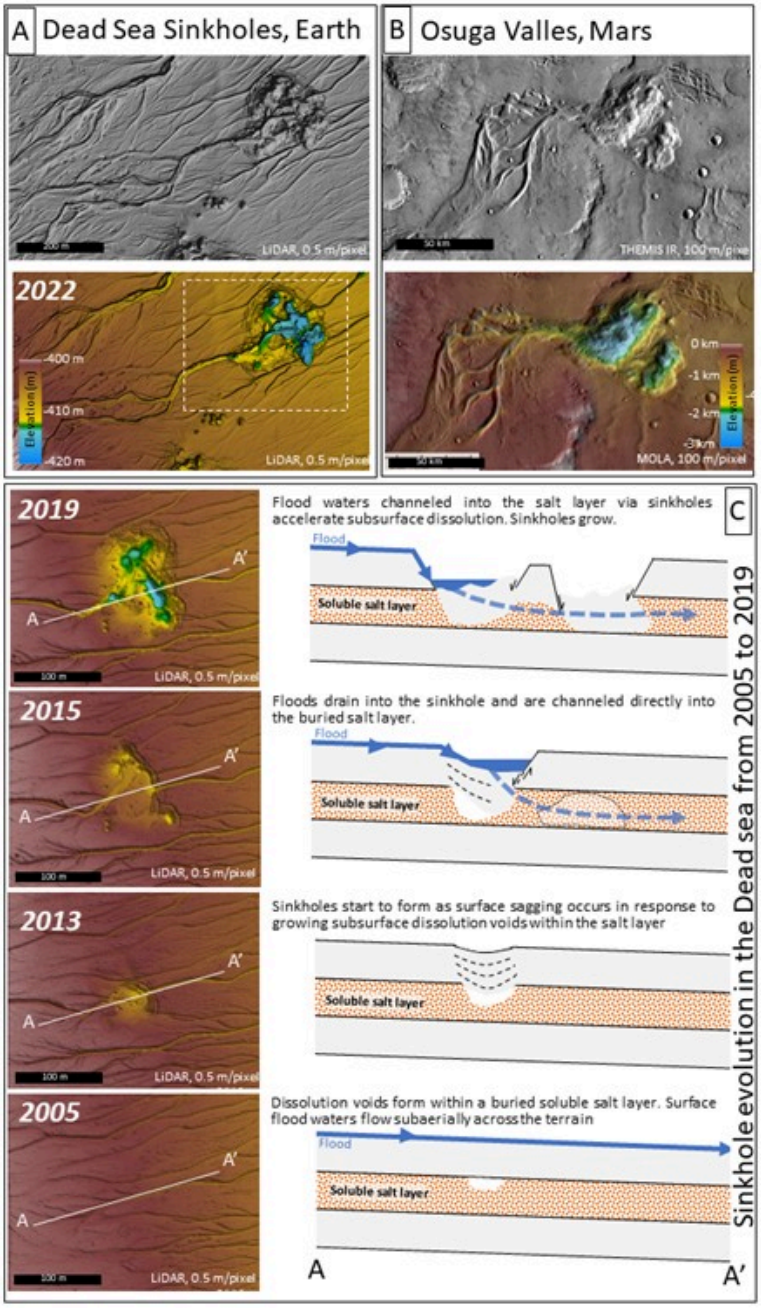

Figure 7

A terrestrial analog site for Osuga Valles. (A) The Dead Sea sinkhole site (31.34° N, 35.41° E). Top: Shaded relief image of the sinkhole site. Bottom: Colorized terrain model. Both are based on airborne LiDAR acquired in 2022. The dashed white rectangle shows the area in panel C. (B) Osuga Valles. Top: THEMIS daytime IR image for Osuga Valles, Mars (15° S, 38° W). Bottom: Colorized terrain from MOLA topography. (C) Sinkhole evolution at the Dead Sea analog sinkhole site from 2005 to 2019. Left: Colorized terrain models. Elevation key same as in A. Right: conceptual model for accelerated sinkhole growth following infiltration of flood waters into a subsurface salt layer facilitated by a sinkhole that captured flood waters.

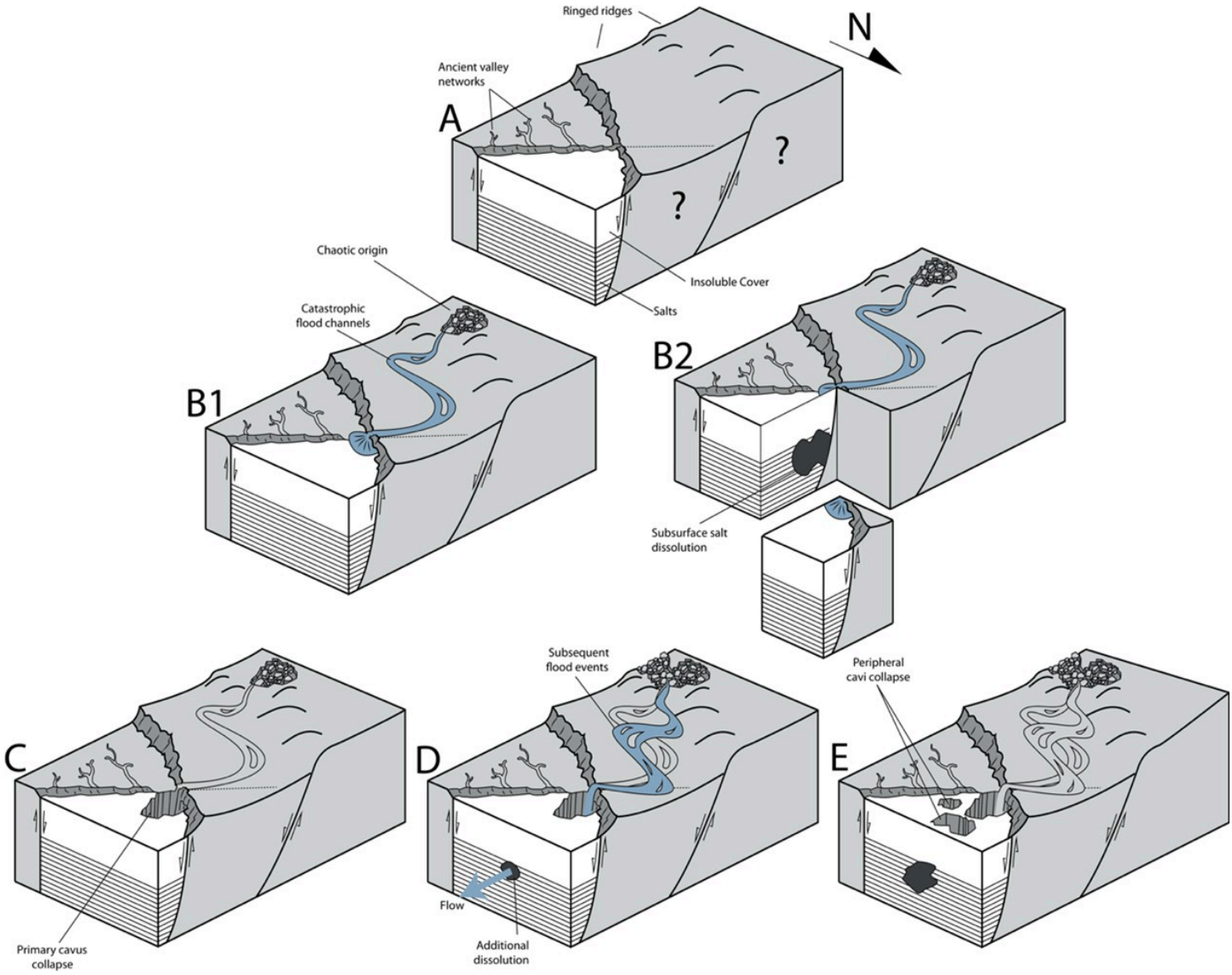

Figure 8

Proposed model for Osuga system formation. (A) A sedimentary basin bounded by the inner (eastern) ringed ridge associated with Ladon Basin in the study region and an approximate E-W fracture zone. The stratigraphy of the middle and upper stairs is unconstrained and beyond the scope of the present study. (B1) Relatively low-discharge outflow from a chaotic region on the upper stair carves channels in the middle stair and breaches the inner ringed ridge at the location of the fracture zone to flow down onto the lower stair. At this stage most of the water flows on the surface, but some water infiltrates the subsurface along the intersection of the fault associated with the ringed ridge and the fracture zone. (B2) The infiltrating water dissolves buried salts to form a cavity. (C) Upward propagation of the cavity ultimately leads to collapse of the surface to form the primary cavus, possibly after the flow has ended. (D) Relatively high-discharge outflow from another chaotic region carves new, deeper channels, which merge at the breach of the inner ringed ridge to flow into the primary cavus. Further buried salt dissolution produces cavities down-flow. (E) The cavities lead to surface collapse and formation of the peripheral cavi, with no observed relation to surface inflow or outflow. The nested cavus also formed at this stage and cut the fluvial morphology on the floor of the primary cavus (not shown). Two outflow events are shown, but a greater number of events is possible and supported by the observations.

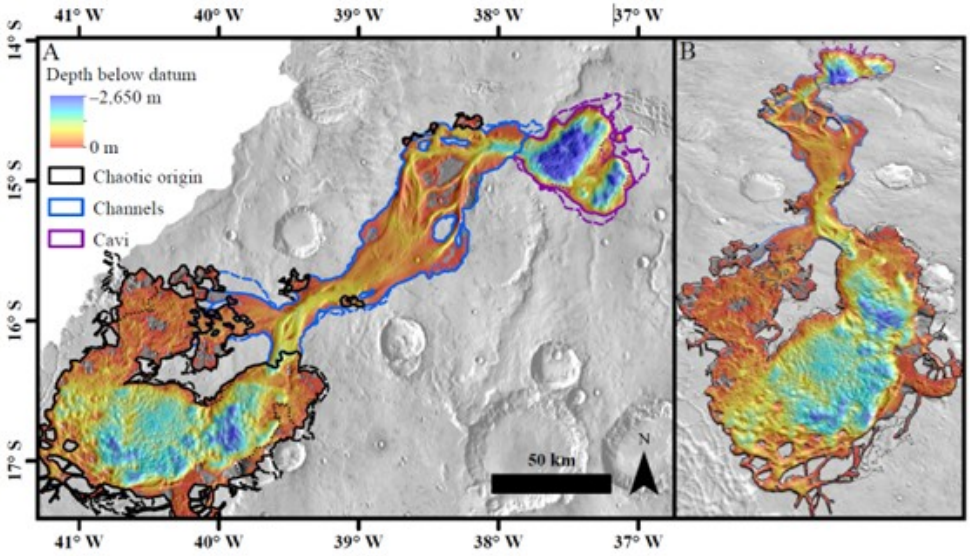

Figure 9

Osuga system's depth relative to its surroundings. (A) The outlines of the three segments (chaotic terrains, channels, cavi) are delineated in different colors. Dashed and dotted lines mark the alternative maximal and minimal boundaries that were used for calculating the uncertainty in each segment's volume, respectively. The depth of the MOLA DTM below its reconstructed pre-erosion surface overlies a THEMIS DAY IR background. The higher opacity background highlights the area within the chosen boundary of the system (i.e., within the solid lines). Note that outlined areas that are not colored according to elevation represent areas where the reconstructed pre-outflow and pre-collapse surface is lower than the MOLA DTM. (B) An east-northeast tilted view. The chaotic origin and the cavi are at the lower and upper part of the image, respectively.

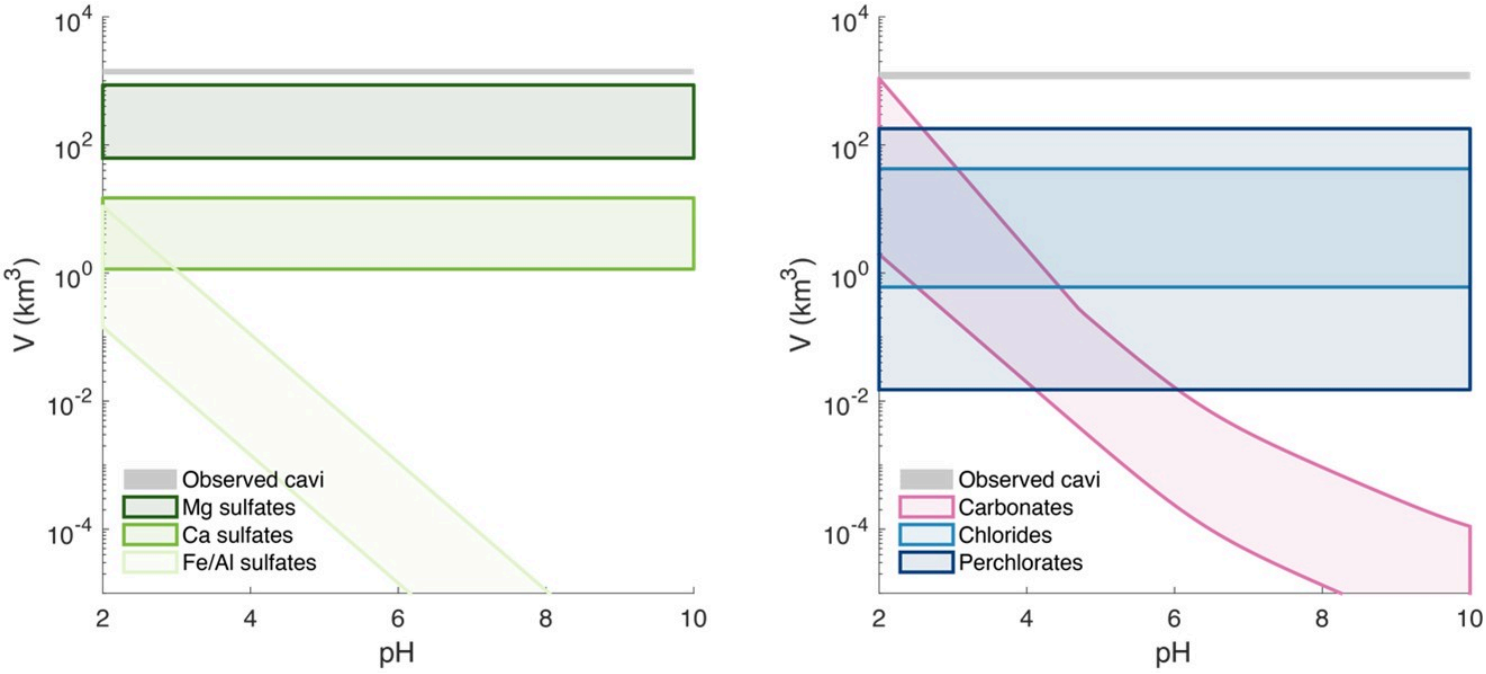

Figure 10

Comparison of observed cavi volume and the potential volume of salt dissolved. The upper gray bars denote the volume of the cavi (see text and Methods), which serves as an estimate for the subsurface volume loss. The colored

envelopes show the volume of salts that could be dissolved by the estimated amount of water that carved the channel system (see text), assuming saturation of the solution with respect to the individual salts (Methods; Table S1).

Supplementary Files

This is a list of supplementary files associated with this preprint. Click to download.

- SupplementaryInformation.docx